In vivo non-invasive monitoring of tissue development in 3D printed subcutaneous bone scaffolds using fibre-optic Raman spectroscopy

Anders Runge Walther [a], Nicholas Ditzel [b], Moustapha Kassem [b], Morten Østergaard Andersen [a], Martin Aage Barsøe Hedegaard [a,*]

[a] SDU Biotechnology, Department of Green Technology, University of Southern Denmark, Campusvej 55, DK-5230 Odense, Denmark
[b] Endocrine Research (KMEB), Department of Endocrinology, Odense University Hospital and University of Southern Denmark, J.B. Winsløws Vej 25, DK-5000 Odense, Denmark

ARTICLE INFO

ABSTRACT

The development of novel biomaterials for regenerative therapy relies on the ability to assess tissue development, quality, and similarity with native tissue types in *in vivo* experiments. Non-invasive imaging modalities such as X-ray computed tomography offer high spatial resolution but limited biochemical information while histology and biochemical assays are destructive. Raman spectroscopy is a non-invasive, label-free and non-destructive technique widely applied for biochemical characterization. Here we demonstrate the use of fibre-optic Raman spectroscopy for *in vivo* quantitative monitoring of tissue development in subcutaneous calcium phosphate scaffolds in mice over 16 weeks. Raman spectroscopy was able to quantify the time dependency of different tissue components related to the presence, absence, and quantity of mesenchymal stem cells. Scaffolds seeded with stem cells produced 3–5 times higher amount of collagen-rich extracellular matrix after 16 weeks implantation compared to scaffolds without. These however, showed a 2.5 times higher amount of lipid-rich tissue compared to implants with stem cells. *Ex vivo* micro-computed tomography and histology showed stem cell mediated collagen and bone development. Histological measures of collagen correlated well with Raman derived quantifications (correlation coefficient *in vivo* 0.74, *ex vivo* 0.93). In the absence of stem cells, the scaffolds were largely occupied by adipocytes. The technique developed here could potentially be adapted for a range of small animal experiments for assessing tissue engineering strategies at the biochemical level.

Introduction

The ability to engineer the regeneration of living tissue has the potential to revolutionize patient care and promise the solution to diseases of chronic tissue degeneration in an ageing world population [1]. Furthermore, regenerative medicine offers several potential clinical opportunities such as regeneration of bone, cartilage, skin, central nervous system and muscular heart tissue [2]. A typical approach in tissue engineering (TE) involve the use of stem cells seeded onto scaffolds in which mechanical, physical, chemical and biological properties are optimized to promote tissue regeneration [1,3,4]. A variety of specialized biodegradable scaffolds facilitating and directing cell proliferation, differentiation and secretion of extracellular matrix are currently subject to extensive research and range from porous calcium phosphate scaffolds [3,5,6] and bioactive glasses [7–9] to biopolymers such as hydrogels [10–13] and collagen scaffolds [3,14]. Furthermore, additive manufacturing, such as 3D printing, is a promising tool for the production of customized patient tailored scaffolds [15]. The development and validation of such

novel smart materials and strategies for tissue regeneration relies on the ability to assess tissue development, quality, and similarity with native tissue types in *in vivo* experiments. Non-invasive imaging modalities such as computed tomography (CT), magnetic resonance imaging (MRI) and ultrasound imaging are applicable in the study of calcified and soft tissues *in vivo* providing good spatial resolutions but limited biochemical information [16]. The ability to monitor tissue regeneration and composition at the biochemical level would greatly improve the development of novel TE strategies [16]. Spontaneous Raman spectroscopy is a non-invasive, label-free, and non-destructive optical technique widely applied for biological characterization. It has been utilized in several biomedical applications owing to the molecule-specific spectral bands of *e.g.* DNA, RNA, proteins, and lipids [17] which provide a basis for optically probing molecular changes associated with diseases [18–22], single-cell spectral imaging [23], and bone/cartilage tissue composition studies [24,25] to name a few. Raman spectroscopy relies on the interaction of photons with sample molecules in which a part of the incoming photon energy is transformed into molecular vibrations. The result is a scattered photon typically with lower energy than the incoming photon. The energy shift can be detected and analysed using spectrographs with a charge coupled device (CCD) camera producing a molecular fingerprint of the sample under consideration in the form of a spectrum (*i.e.*

* Corresponding author at: Campusvej 55, DK-5230 Odense, Denmark.
  E-mail address: marhe@igt.sdu.dk (M.A.B. Hedegaard).

photon counts in a range of energy shift). The method holds great potential in a number of applications in tissue engineering such as monitoring stem cell differentiation [26–28], bone regeneration [29–31], *in vitro* tissue formation in scaffolds [32,33], assessment of transplant/scaffold quality and composition [34–36], and organ transplantability [16]. So far Raman spectroscopy has been applied in the field of tissue engineering and regenerative medicine (TERM) in mostly *in vitro* [32-35,37-41], *ex vivo* [42] and proof of concept studies [29,31,33]. A single study on live animals demonstrating the ability to spectrally distinguish healthy and compromised oral mucosa TE constructs post implantation has been reported although the monitoring procedure involved temporary removal of overlying tissue on the live animals [43].

Experimentally induced ectopic bone formation is a well described entity and is commonly achieved through transplantation models typically involving a scaffold carrying cells with or without the addition of bone stimulating agents such as bone morphogenic protein 2 (BMP2) [44–46]. The analyses of such models are crucial to understanding osteogenic differentiation of cells independent from an osseous environment and important in the field of skeletal tissue engineering for optimizing bone formation [47]. Time resolved analysis of ectopic bone formation in animals at the biochemical level can be addressed by biochemical assays and histological staining of tissue sections at discrete timepoints, however these methods are inherently invasive, destructive and require several sacrifices for quantitative analysis [48].

In this paper we explore the use of Raman spectroscopy for *in vivo* non-invasive, non-destructive and label-free monitoring of tissue formation in calcium-phosphate scaffolds implanted subcutaneously in mice. Using a fibre-optic Raman probe we follow the spectral variations related to tissue formation in the scaffolds over 16 weeks. We address the potential use of Raman spectroscopy to monitor and quantify statistically significant differences in the biochemical composition of tissue under different TE strategies including scaffolds loaded with and without mesenchymal stem cells (MSCs). To our knowledge this is the first demonstration of Raman spectroscopy based non-invasive and label-free *in vivo* monitoring of TE scaffolds. We believe the approach described here can be further developed and tailored for any small animal subcutaneous implant model to study ectopic bone formation, tissue regeneration, scaffold resorption dynamics and comparison of TE strategies at the biochemical level, ultimately improving the development of novel regenerative therapies and reducing the number of animals needed for longitudinal studies in this context.

Methods

Ethics and approval

All *in vivo* experiments were performed under the permission from the National Danish Animal experiments inspectorate (2017–15–0201–01210). Danish regulations for care and use of laboratory animals were maintained throughout the experiment period. Experiments complied with European legislation and associated guidelines for animal experiments. ARRIVE guidelines [49] for animal experiments were followed.

3D printed scaffolds

3D printed scaffolds of medical grade β-tricalcium phosphate (βTCP) [50] in the shape of discs Ø8 mm, 3 mm thick and 30% rectangular infill pattern (Supplementary Fig. S1A), were purchased from Particle3D. The scaffolds have previously been shown to support cell adhesion and growth *in vitro* and *in vivo* [50,51]. The prints were autoclaved prior to cell seeding. The β polymorph of the tricalcium phosphate was checked before and after the 3D printing procedure by X-ray diffraction (XRD) using a PANalytical X'pert Pro-x-ray diffractometer equipped with a Cu Kα source. XRD was collected in reflection using the Bragg-Brentano configuration (Supplementary Fig. S4A).

In vivo *bone formation in immunodeficient mice*

To obtain ectopic bone formation in scaffolds in live mice, we used a well-characterised, immortalised, luciferase and telomerase expressing, human mesenchymal stromal cell line (hMSC) [52–55] cultured in minimal essential medium (MEM) (cat.nr. 31095, Gibco) containing 10% foetal bovine serum and 1% penicillin-streptomycin. The expression of luciferase allowed for continuously monitoring the presence and location of hMSCs using bioluminescence imaging. Cells were incubated in 5% CO_2 incubators at 37 °C and 95% humidity. The cells were seeded on the sterile βTCP scaffolds placed in low adhesion 24 well plates (Nunclon Sphera, ThermoFisher) by adding 100 µl medium containing the cells to the top surface of the scaffold. The scaffolds were then left to settle in the incubator for 1.5 h followed by the addition of 1 ml medium with or without growth factor (GF); 100 ng/ml BMP2 (PeproTech). Scaffolds without cells were treated similarly with culture medium only. The scaffolds and cells (passage 47) were then incubated for 24 h prior to subcutaneous implantation (Supplementary Fig. S1B) in five experimental units ($n = 5$); female CIEA NOG mice, 2 months old (Taconic). After receiving the mice, they were allowed to acclimatize for two weeks before the experimental period. To mimic different TE strategies, we tested four different experiment conditions; without hMSCs (no cells), 7.5×10^5 cells/scaffold + 24 h BMP2 preconditioning (MSC$_{7.5}$+GF), 1.5×10^5 cells/scaffold (MSC$_{1.5}$) and 7.5×10^5 cells/scaffold (MSC$_{7.5}$). Scaffolds were randomly assigned to the experimental groups. Each mouse received all four conditions by implantation in four subcutaneous pockets in the dorsal region [56]. All mice were kept in the same cage and fed *ad libitum*. Sixteen weeks after implantation the mice were euthanized by cervical dislocation and the scaffolds were removed, fixed in 10% neutral buffered formalin (4% formaldehyde) for one day at room temperature and stored in phosphate buffered saline at 4 °C until further use.

In vivo *bioluminescence*

Survival and localization of hMSC in scaffolds were evaluated using bioluminescence imaging of the mice with an IVIS spectrum system (Perkin Elmer). Cell mediated D-luciferin bioluminescence imaging was conducted two days after transplantation of scaffolds and regularly for the duration of the experiment. The mice received 0.1 ml pr. 10 mg body weight D-Luciferin solution (15 mg/ml in PBS) through intra-peritoneal injection 10–15 min prior to imaging. The mice were anesthetized with isoflurane during imaging. Bioluminescence measurements were conducted after Raman measurements to ensure that the presence of D-luciferin would not produce interfering spectral signals.

Micro-computed tomography (µCT)

All scaffolds were scanned prior to cell seeding and after termination and removal from the animals with a high-resolution µCT system (vivaCT40; Scanco Medical) resulting in three-dimensional reconstructions with cubic voxel sizes of $10.5 \times 10.5 \times 10.5$ µm^3.

Raman spectroscopy instrumentation

The fibre-optic Raman system (Fig. 1a) used for *in vivo* transcutaneous monitoring of TE scaffolds consists of a near-infrared (NIR) multimode diode laser emitting at a wavelength of 785 nm (B&W TEK Inc.). This wavelength, has previously been reported to lie in the optimal range for low light extinction in tissue [57–59]. The laser was fibre-coupled into the excitation terminal of a flat faced tip Raman filtered fibre-optic probe (EmVision LLC). The probe consists of eight 300 µm core, low OH 0.22 NA optical fibres, a single excitation fibre centred in a ring of 7 collection fibres. The probe tip contains a doughnut shaped long pass filter for suppression of Rayleigh scattered light and a circular laser band pass filter for the removal of unwanted spectral emissions
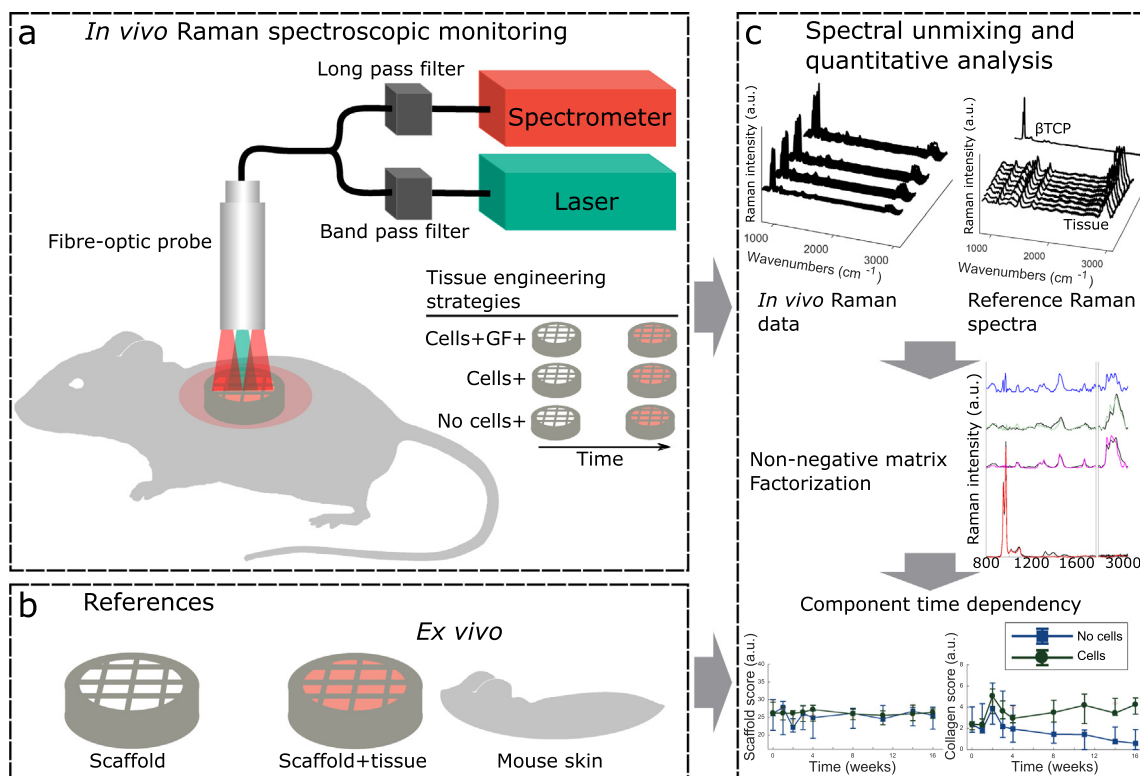
Fig. 1. Schematic of the Raman spectroscopy system, multivariate spectral unmixing and analysis for *in vivo* biomolecular monitoring of TE scaffolds. **(a)** Fibre-optic Raman spectroscopy allows for facile, non-invasive and label-free assessment of subcutaneously implanted scaffolds in live mice. Inelastic scattered laser light is collected by the spectrometer producing a molecular fingerprint of specimens within the sampling volume (overlap region of green and red cones). Performing spectral unmixing on the combined data matrix of pure reference **(b)** and *in vivo* spectra **(a)** allows for isolating spectral observations related to scaffold material, skin and developing tissue for all timepoints **(c)**.

from the laser and fibres. The probe tip is terminated by a glass window. Furthermore in-line laser band pass and long pass filters (Semrock) were utilized between laser to probe and probe to spectrometer. Raman scattered light collected from the probe were directed to the 0.3 NA, transmission grating based Eagle Raman-S spectrometer (20 μm slit) (Ibsen Photonics) integrated with an iVAC 316, Peltier cooled (−65 °C), back-illuminated, deep depletion charge coupled device (CCD) (Andor, Oxford Instruments) with a spectral resolution of ∼3.5 cm^{-1} (determined as full width at half maximum of mercury argon emission lines). The spectrograph wavelength axis was calibrated using the mercury argon lamp and regularly checked using a polystyrene sample. The combination of NIR laser wavelength and Raman volume probe was chosen to ensure a sampling depth in the millimetre range [60].

Raman data collection

Transcutaneous Raman spectra of scaffolds representing different TE strategies were acquired two days after implantation and regularly during the 16-week period. Each spectrum was measured with an acquisition time of 10–20 s using 6 or 3 accumulations respectively with 20 mW at the sample. Measurements were collected in a blinded manner. The distance between probe tip and mouse skin was kept at 3 mm using a spacer giving an approximate laser spot diameter of 4.5 mm covering a substantial portion of the scaffolds, while resulting in a laser intensity at the skin lower than the maximum permissible value for human exposure to artificial optical radiation in EU [61]. In addition, we have previously shown that contributions from surface Raman and autofluorescence signals to the overall spectrum can be mildly suppressed by increasing the distance from the probe to the sample [62]. The probe was positioned approximately above the centre of the disc shaped scaffolds. The outline of the implants was clearly visible as the skin formed

a close fit around the underlying scaffolds. Before measurements, the mice were anesthetized with 3.5% isoflurane in pure oxygen and the fur was removed locally at the position of the underlying scaffold. During measurements, the mice continuously received isoflurane (2% in pure oxygen). The dark chamber of the IVIS system with built in isoflurane outlets was used for all Raman measurements. A graphical user interface (GUI) was developed to interface with the spectrometer CCD and enable data collection using MATLAB (Mathworks Inc.) programming environment and a software development kit (Andor, Oxford Instruments). Reference spectra of fixed, *ex vivo* scaffolds, and tissue were obtained at four locations on each scaffold with the Raman fibre-optic probe in close proximity (<1 mm) from the surface using 50 mW laser power and 3–4 s acquisition time. Fifteen skin Raman reference spectra were collected from the 5 euthanized mice by removing the skin at the location of scaffolds and placing it on aluminium substrates. The Raman probe was positioned in close proximity to the sample and spectra were collected using 20 mW laser power, 10 s acquisition time and 6 accumulations. Reference spectra of medical grade βTCP powder (Particle3D), printed βTCP scaffolds and laboratory grade collagen (CAS: 9007–34–5, Sigma-Aldrich) were collected using 50 mW laser power, 10 s with 3 accumulations, 10 s with 1 accumulation and 5 s with 20 accumulations, respectively.

Spectral data processing and analysis

All data analysis was performed in locally written algorithms in MATLAB environment. To remove tissue autofluorescence, spectra were subject to baseline subtraction using a Whittaker filter with an asymmetric least squares algorithm [63–65]. This was followed by cosmic ray removal [66], smoothing using a 2nd order, 5 point window Savitzky-Golay filter to reduce random spectral variations related to noise, and

Table 1
Band assignments for Raman spectra.

Raman shift/cm^{-1}	Band assignment
850–880	Tyrosine, proline, hydroxyproline [17,24,72], and C–O-O mode of lipids [73]
950, 972, 1000–1110	PO$_4^{3-}$ stretch modes [74]
1005	Ring breathing mode of phenylalanine [75]
1220–1350 cm^{-1}	Protein Amide III [72]
1304	Lipid CH$_2$ twist [73]
1445	Protein and lipids CH$_2$ deformation [72,73]
1590–1700	Protein Amide I [72]
1658	C = C stretch mode of lipids [73]
2750–3050	Lipid and protein C–H, CH$_2$ and CH$_3$ stretch vibrations [17,73]

relative intensity correction using NIST SRM 2241 (National Institute of Standards and Technology) [67]. To account for day-to-day instrument variations all spectra were normalized to the intensity (area) of the internal Raman band at 407 cm^{-1} of the probe. This approach ensured that fluctuations in delivered laser power from equipment and bending of optical fibres did not influence the measurements [68,69] while allowing for the absolute intensities of spectral features to be used as input to multivariate data analyses. *In vivo* and *ex vivo* scaffold spectra were subject to spectral interference subtraction to further remove fluorescent spectral contributions (Supplementary Fig. S4B) originating from metal impurities in the calcium phosphate mineral structure [70]. This was accomplished by estimating the fluorescent spectral contribution in the range (1100–2040 cm^{-1}) using multivariate statistical modelling [33] on all scaffold spectral observations including βTCP powder and 3D printed implant references (Supplementary Fig. S5).

Following pre-processing, spectral models were developed using the MATLAB statistics toolbox function non-negative matrix factorization (NNMF) [71] (Fig. 1c) with *in vivo* spectra (Fig. 1a), *ex vivo*, and reference spectra (Fig. 1b) as input. The method assumes every biochemically complex spectral observation can be described by a linear combination of pure component spectra [65] related to *e.g.* βTCP, skin, bone and connective tissue. The factorization produces non-negative model spectra along with their relative contributions to the observations as scores. Raman bands characterising the spectral observations in the present work are summarised in Table 1.

Histology and immunohistochemical analysis

Upon completing Raman and μCT measurements, the fixed scaffolds were decalcified in formic acid (4 M) for 3 days and subsequently dehydrated in standard increasing concentrations of ethanol, ending in xylene before paraffin embedding. Sections were stained with Hematoxylin and Eosin (H&E), stained against human vimentin for visualisation of hMSC mediated tissue using anti-vimentin antibody (purchased from Abcam) or stained with Pico Sirius Red (PSR) for visualisation of collagen content. Histological sections (4 μm) were cut at an approximate depth of 200 μm from the top of the scaffold and imaged through a 10X microscope objective using an automated conventional brightfield microscope (Leica DM4500B, Leica Microsystems) and Surveyor software (Objective Imaging). Images were recorded and stitched together to produce micrographs of entire implant sections. Quantification of collagen content in PSR images was performed using the ImageJ software package. All images were converted to an RGB stack and presented in grey scale with intensity values from 0 to 255. The green channel was used for thresholding with upper and lower threshold set to 95 and 19 respectively. The total collagen positive area was then measured and divided by the total length of the scaffold cavity perimeters producing an area-to-perimeter ratio. The outer edges of the scaffolds were not included in this analysis. The lengths of the cavity perimeters were estimated manually using the freehand selection tool in imageJ (Supplementary Fig. S7). Tissue processing, microscopy and image analysis were performed blinded until completion.

Statistical analysis

One and two-way analysis of variance with post hoc multiple comparisons using the Dunn-Sidak approach were used when comparing more than two experimental groups of five biological replicates ($n = 5$) to test for group effects, time effects and interactions. Wilcoxon Rank Sum test was used for comparison of two experimental conditions. Significance levels are indicated as * $p<0.05$; ** $p<0.01$; *** $p<0.001$. Time resolved data are presented as the median with error bars indicating 0.25 and 0.75 quantiles. Variable correlations were assessed using Pearson's correlation coefficient (r). All statistical analyses were performed using MATLAB programming environment. A single spectral datapoint belonging to the group of scaffolds without hMSCs (no cells) at day 0 was excluded from any analysis due to a small saturation of the CCD in the spectral range 950–970 cm^{-1}. The total *in vivo* spectral dataset thus includes 179 spectra acquired at 9 timepoints, from five mice each with four implanted scaffolds.

Results

In vivo *biomolecular monitoring of tissue development in scaffolds*

Bioluminescence imaging showed a stable culture of hMSCs throughout the duration of the experiment located at the position of scaffolds that were initially seeded with cells (Supplementary Fig. S2). The average Raman spectrum $\pm$ 1 standard deviation following pre-processing of all 179 *in vivo* observations of subcutaneous scaffolds (Fig. 2a) is dominated by the spectral features related to βTCP and mouse skin as seen by comparison with reference spectra (Fig. 2b). The most prominent peaks at 950 cm^{-1} and 972 cm^{-1} belong to the βTCP PO$_4^{3-}$ stretch vibration. Typical Raman protein and lipid bands are visible in the fingerprint and high wavenumber (HW) region (800–1750 cm^{-1} and 2750–3050 cm^{-1} respectively). The 1005 cm^{-1} ring breathing mode of phenylalanine overlaps with the weaker PO$_4^{3-}$ stretch modes of βTCP (1000–1110 cm^{-1}). The Amide III band (1220–1350 cm^{-1}), 1445 cm^{-1} CH$_2$ deformation, and Amide I band (1590–1700 cm^{-1}) of protein is superimposed with the CH$_2$ twist at 1304 cm^{-1}, 1445 cm^{-1} CH$_2$ deformation, and 1658 cm^{-1} C=C stretch mode of lipids. The band in the HW region is assigned to lipid and protein C–H, CH$_2$ and CH$_3$ stretch vibrations where the 2850 cm^{-1} and 2888 cm^{-1} peaks (CH$_2$ stretch) gains a high contribution from the presence of lipids.

Spectral unmixing and quantitative analysis

The probe position with respect to the underlying skin and scaffold, remaining mouse fur, biological variation, as well as respiratory movement during measurements, are all sources of variation that can masque any time correlated and engineering strategy dependent spectral variation related to tissue development. To accommodate this and extract the spectral information related to tissue formation, we performed factor analysis following pre-processing (see "Methods" for more detail) on a spectral dataset including *in vivo* spectra, references acquired from
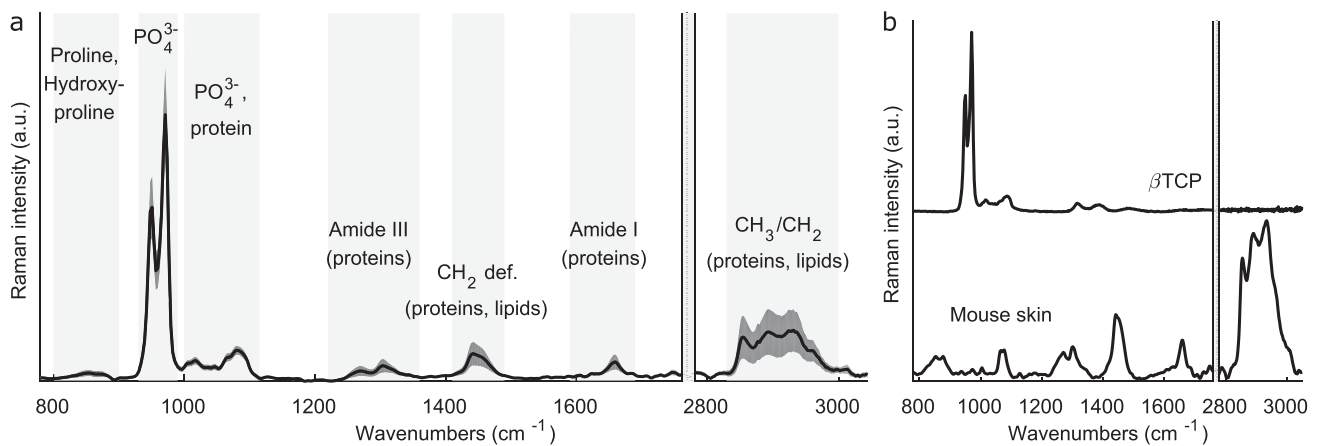
Fig. 2. *In vivo* Raman spectral observations and reference spectra. **(a)** Average (solid line) $\pm$ standard deviation (shaded region) of all *in vivo* transcutaneous Raman observations after preprocessing. Spectra were collected at the location of implanted scaffolds using the fibre-optic volume probe. Mice were shaved prior to spectral acquisition. Prominent peaks are related to β tricalcium phosphate (βTCP), protein and lipid vibrational modes. **(b)** Reference spectra of βTCP scaffold collected prior to cell seeding and implantation along with mouse skin reference. The silent spectral region (1750–2750 cm^{-1}) is excluded from the plots as it contains no relevant biochemical information for this application.

pure scaffolds, excised mouse skin, and spectra of scaffolds excised after sacrificing the mice. The factor analysis was performed using the non-negative matrix factorization (NNMF) algorithm available in the MATLAB software package. The algorithm creates a lower rank estimate of the original data matrix resulting in pure spectra representing different biochemical components and their contribution to the original spectral observations given as scores. This enabled time-resolved visualisation of the multivariate spectral contributions from tissue and quantitative statistical comparison between timepoints and TE strategies (Fig. 3). A four-component model produced biochemically meaningful component spectra corresponding to βTCP, mouse skin, collagen-rich and lipid-rich proteinaceous tissue (component 1–4 respectively, Fig. 3a). Components 1 and 2 have correlation coefficients 0.99 and 0.97 with the respective references. Component 3 is highly similar (correlation coefficient 0.96) to the spectrum of a laboratory grade collagen reference which was not included as input to the NNMF algorithm. Component 4 exhibits slightly imperfect separation of spectral signatures a seen from the 950–972 cm^{-1} contribution from βTCP, however exhibits features related to lipids by correlation with previously published work (Table 1). The contribution from each model component to the individual *in vivo* spectral observations can be assessed through the component scores (Fig. 3b). Spectral components that are related to tissue formation may exhibit a relative change in scores over time as the content of tissue changes. In contrast, components unrelated to tissue formation would exhibit random variations with time. Indeed, both the βTCP and skin component scores exhibit little or no time-related change however, both the collagen and lipid rich components show time-correlated tendencies (Fig. 3b). In addition, component 3 and 4 scores show a dependency on engineering strategy. Scaffolds without hMSCs show an overall decrease in relative expression of collagen over time in contrast to scaffolds with hMSCs showing an overall increase. Scaffolds without hMSCs develop bone when they are placed in bone defects where native MSCs are abundant, but these are absent in the ectopic implantation site used here which may explain why these implants fail to form collagen rich bone tissue. Differences between initially acellular and cellular scaffolds are also apparent for scores of the lipid rich tissue component, possibly due to the subcutaneous fat layer growing into the empty scaffolds. Scaffolds with hMSCs follow similar mild increase in scores over time whereas scaffolds without shows a more rapid increase in the score values. A two-way ANOVA on the scores for timepoints 0 and 16 weeks across all groups revealed a statistically significant interaction between time and engineering strategy for component 3 and 4 ($p<0.006$ and $p<0.001$ respectively) while no statistical significance were found

for component scores 1 and 2 on either interaction or across factors levels.

Following the significant interaction for scores of components 3 and 4 across time and experimental condition, we investigated the differences within each group or timepoint, since no superposition of factors can be justified. A one-way ANOVA on scores of component 3 across scaffold groups at the 16 weeks timepoint followed by post hoc multiple comparison (Dunn-Sidak approach) revealed a statistically significant difference between scaffolds containing hMSCs and scaffolds without (Fig. 3c). In scaffolds with hMSCs the amount of collagen-rich tissue was 3 to 5 times higher than scaffolds without. A significant difference between cellular and initially acellular scaffolds was also observed for the scores of component 4 at 16 weeks (Fig. 3c). Here the amount of lipid-rich tissue was estimated to be ~2.5 times higher in scaffolds without hMSCs. Focusing on timepoints 0 and 16 weeks, scaffolds seeded with a high number of cells (7.5×10^5) had a statistically significant increase in collagen-like content from 0 to 16 weeks as revealed by Wilcoxon Rank Sum test. All the groups showed a statistically significant increase in lipid rich tissue from 0 to 16 weeks while scaffolds without cells showed the largest difference. The highest average expression of collagen-rich extracellular matrix was observed after 16 weeks of implantation in scaffolds seeded with hMSCs preconditioned with BMP2 although not statistically significantly different from the other scaffold groups seeded with cells.

Histology and micro computed tomography of ectopic bone

To confirm the spectral observations, we conducted μCT and histology of explanted scaffolds. The histological analysis shows the presence of ectopic bone in all scaffolds that initially received hMSCs as indicated by the osteocytes (purple spots) enclosed in dense extracellular matrix (red colour from H&E stain, Fig. 4a and Supplementary Fig. S3). Staining against human vimentin (Fig. 4a, hVim, brown colour) confirmed that the ectopic bone originates from the hMSCs and is not formed by cells from the host. Both hMSCs and bone embedded individual osteocytes show a positive expression of hVim. In contrast, scaffolds without hMSCs (no cells) show the presence of hVim negative adipocytes in the scaffold cavities (Fig. 4a, H&E, hVim, and Supplementary Fig. S3). These results are in excellent agreement with the Raman spectroscopic analysis which indicated a high content of a lipid rich tissue type for this group and a collagen rich tissue type for scaffolds seeded with hMSCs.

In addition, the presence of calcified tissue in scaffolds initially seeded with stem cells was confirmed by the μCT images, showing in-
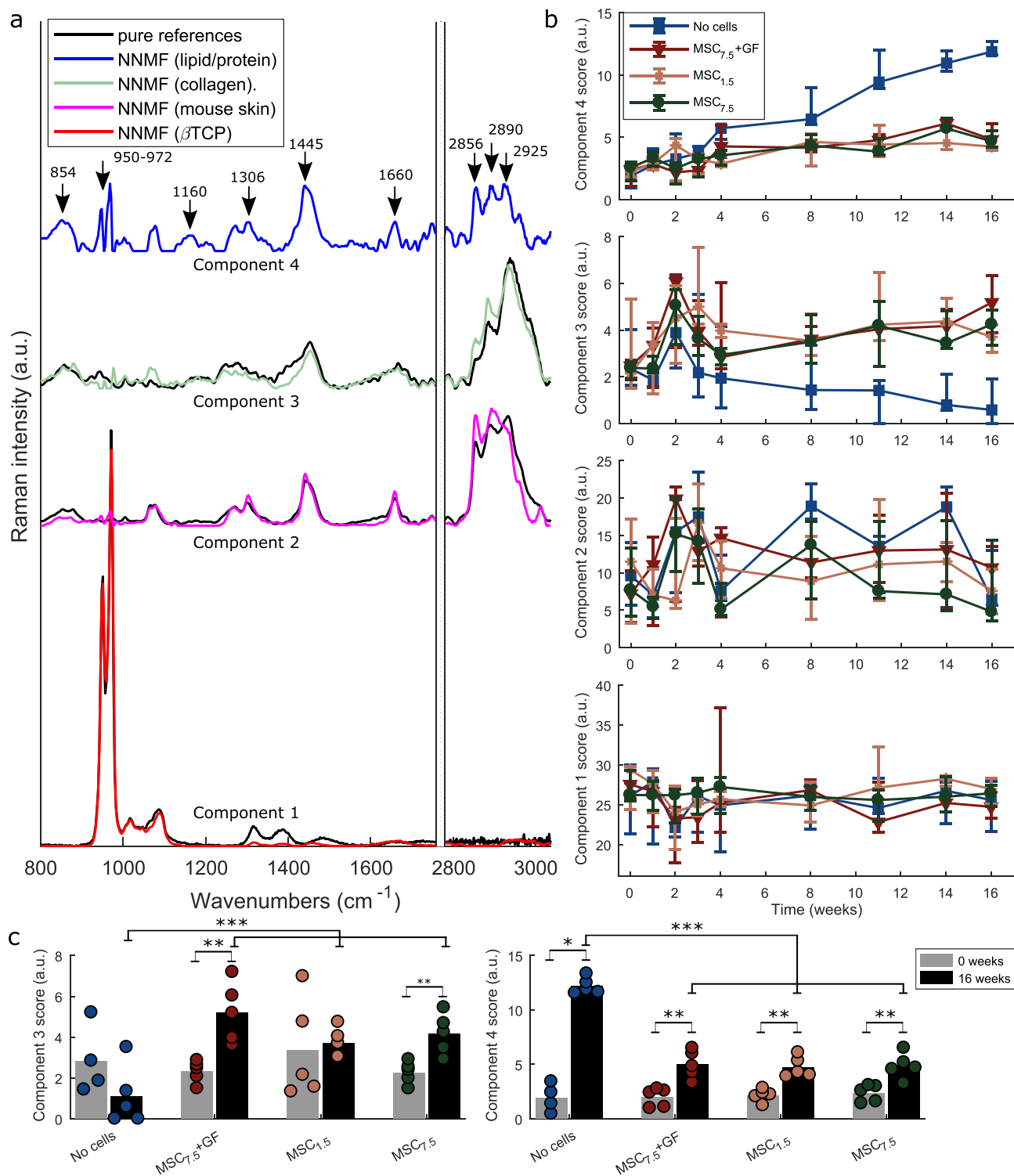
Fig. 3. Non-negative matrix factorization analysis of *in vivo* spectral observations. **(a)** Model spectra developed on Raman dataset including *in vivo* observations, *β* tricalcium phosphate (*β*TCP) powder, preimplantation *β*TCP scaffolds, ex vivo *β*TCP scaffolds and mouse skin references. The silent region (1750–2750 cm^{-1}) has been excluded from the plot as it contains no relevant spectral information for this application. Model spectra (component 1–3) correlate well with pure references showing *β*TCP, mouse skin and collagen respectively. Component 4 was identified as a proteinaceous, lipid rich tissue component through spectral assignments (black arrows) with a *β*TCP feature around 950–972 cm^{-1} related to imperfect spectral model separation. **(b)** Scores as function of time of *in vivo* observations for each component in (a) according to spectral similarity. Plots show median (datapoint) along with 0.25 and 0.75 quantiles (error bars) for each experimental group with five biological replicates ($n = 5$). Groups represent subcutaneous implants without mesenchymal stem cells (■), seeded with mesenchymal stem cells (MSC); 1.5×10^5 and 7.5×10^5 pr. implant (✳, ●) and 7.5×10^5 MSCs pr. implant preconditioned for 24 h with growth factor (GF) bone morphogenic protein 2 prior to implantation (▼). Lines are included as approximate guides connecting the datapoints. **(c)**, Statistical analyses of component 3 and 4 scores for timepoints 0 and 16 weeks, average score (bar graphs) are shown along with data points. One-way analysis of variance with post hoc multiple comparison (Dunn-Sidak approach) was used for comparing more than two groups at the 16 weeks timepoint. Wilcoxon Rank Sum test was used for comparison of scores at timepoints 0 and 16. $^*p<0.05$, $^{**}p<0.01$, $^{***}p<0.001$.
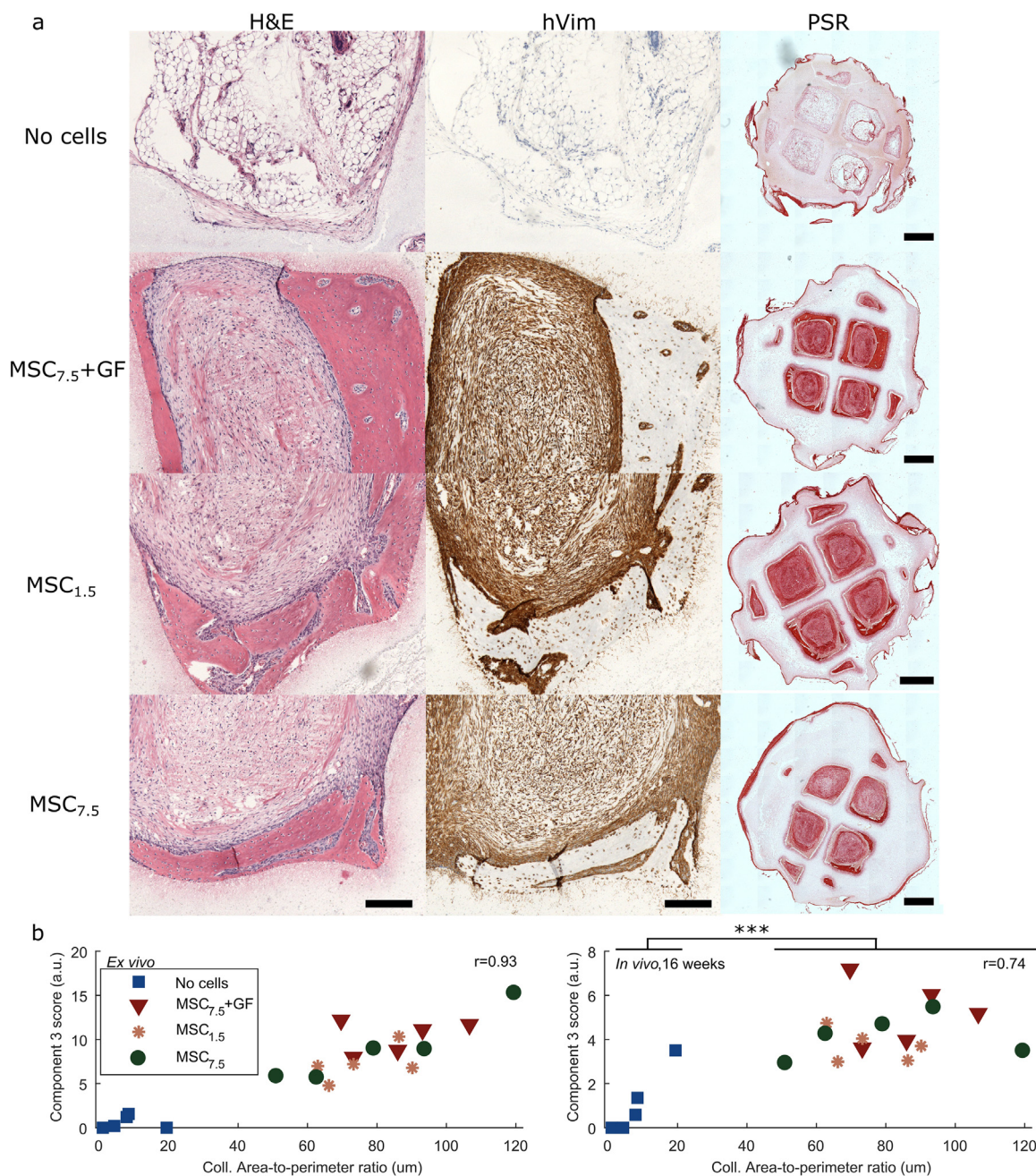
Fig. 4. Histology and immunohistochemical analysis of explanted scaffolds. **(a)** Representative micrographs of histological sections showing Hematoxylin/Eosin (H&E), human vimentin (hVim) and Pico Sirius Red (PSR) stains after 16 weeks subcutaneous implantation in mice. H&E and hVim images are shown at approximately identical locations on the samples. PSR images represent entire scaffolds by stitched together micrographs. **(b)**, Quantitative analysis of collagen content from Raman spectroscopy (NNMF Component 3) and PSR images after 16 weeks of implantation. Collagen (Coll.) content from PSR histology is represented by a ratio of total PSR positive area divided by total scaffold cavity perimeter (Area-to-perimeter ratio). Histology derived measures of collagen content correlate well with both *ex vivo* and *in vivo* Raman derived collagen estimates. Pearson's correlation coefficient (r). Scales bars: 200 μm (H&E, hVim micrographs) and 1 mm (PSR micrographs). Groups: scaffolds without (No cells ■) human mesenchymal stem cells (hMSCs), with hMSCs (MSC$_{1.5}$ ✳, MSC$_{7.5}$ ●, MSC$_{7.5}$+GF ▼) amount indicated by subscript (*e.g.* 7.5 = 7.5×10^5 cells per scaffold). hMSCs preconditioned with BMP2 growth factor for 24 h prior to implantation (+GF).

growth of bone into the scaffold cavities (Fig. 5). Next, we asked whether a semi-quantitative histomorphometric analysis based on the well know collagen specific Pico Sirius Red (PSR) stain would support the Raman spectral quantifications of scaffold collagen content observed *in vivo* and *ex vivo* after 16 weeks of implantation. The collagen content from PSR was determined by intensity thresholding micrographs of entire PSR stained scaffolds (Fig. 4a, PSR and Supplementary Fig. S6). The total PSR positive area (μm^2) was then measured and normalized to the to-

tal perimeter (μm) of cavities for each scaffold (Supplementary Fig. S7). These area-to-perimeter ratios (μm) were then plotted against the individual *ex vivo* and *in vivo* Component 3 scores representing the Raman spectroscopy derived collagen content (Fig. 4b). A significant correlation between histology and Raman-based estimates was found for both *ex vivo* (r = 0.93, p<0.0001) and *in vivo* (r = 0.74, p<0.001) spectral observations after 16 weeks of implantation. The lower correlation coefficient related to the *in vivo*, 16 weeks spectral observations compared to
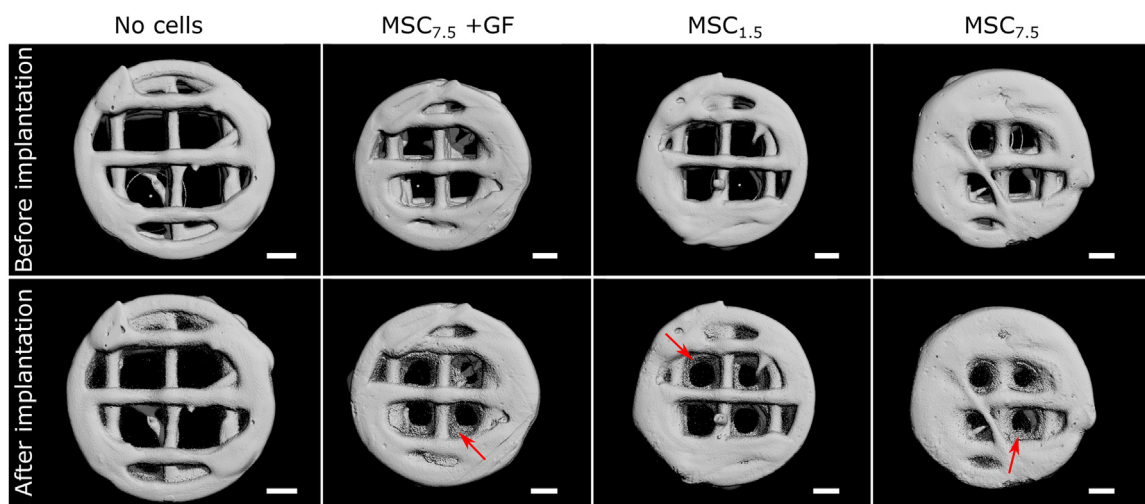
Fig. 5. Micro-computed tomography of scaffolds before and after implantation. Representative images of μCT reconstructions of four different scaffolds before and after 16 weeks subcutaneous implantation in mice. Scaffolds were seeded with (MSC) and without (No cells) human mesenchymal stem cells with amount indicated by subscript (*e.g.* $7.5 = 7.5 \times 10^5$ cells per scaffold). hMSCs preconditioned with BMP2 growth factor for 24 h prior to implantation (+GF). Arrows exemplifies areas with ingrowth of calcified tissue. Scalebars: 1 mm.

ex vivo observations is attributed to the more complicated conditions associated with live animal measurements such as overlying tissue and respiratory movement. On average the collagen content as determined by PSR staining showed the highest amount for scaffolds seeded with BMP2 preconditioned hMSCs (hMSC$_{7.5}$+GF) with a Coll. Area-to-perimeter ratio of 86 μm. The amount was slightly lower (not significant) for scaffolds from the hMSC$_{7.5}$ and hMSC$_{1.5}$ groups with 81 μm and 76 μm respectively while the lowest amount was observed for the acellular scaffolds (8 μm). All groups of scaffolds seeded with hMSCs showed a significantly higher amount of collagen compared to the initially acellular scaffolds (Fig 4b, one-way ANOVA $p<0.0001$, Dunn-Sidak $p<0.001$) reflecting the *in vivo* Raman analysis 16 weeks after implantation (Fig. 3c, Component 3 scores).

Discussion

The ability to follow tissue development in scaffolds *in vivo* using Raman spectroscopy was demonstrated and explored using a set of experimental conditions mimicking different TE strategies. Customized 3D printed βTCP scaffolds [51,76] (Supplementary Fig. S1) were seeded with or without human luciferase and telomerase expressing mesenchymal stem cells (hMSC) [52,54,55]. Four different experimental conditions (TE strategies) were investigated in five immunodeficient mice for 16 weeks. Each mouse received one of each condition by implantation in subcutaneous pockets at the dorsal region (total of four implants per mouse). The conditions include scaffolds without cells (no cells), with low amount of cells (MSC$_{1.5}$), high amount of cells (MSC$_{7.5}$) and scaffolds receiving a high amount of cells preconditioned with bone morphogenic protein 2 (BMP2) prior to scaffold seeding (MSC$_{7.5}$+GF) (see methods). While mesenchymal stem cells have been extensively investigated in the context of skeletal regeneration [77], recombinant BMP2 has been shown to enhance bone formation *in vivo* [78], increase osteogenic differentiation capacity of MSCs under both short [79] and continuous [80] exposure. Together these strategies reflected a set of initial conditions for testing the spectroscopic monitoring system.

We then developed a comprehensive spectroscopic system and experimental workflow for the *in vivo* biomolecular assessment of TE scaffolds. This included the well-established subcutaneous implantation model [47], data acquisition, multivariate spectral unmixing and quantitative analyses (Fig. 1). The fibre-optic approach enabled facile acquisition of Raman spectra compatible with existing dark chambers designed for bioluminescence imaging of live animals. The results demonstrated that

fibre-optic Raman spectroscopy not only can be used to monitor and quantify time dependant tissue formation in subcutaneous TE scaffolds *in vivo* but also provides information about tissue type related to different physiological conditions. The spectral analysis performed in this work, did not include any spectral references for modelling the developing tissue. Instead, the tissue components were extracted in an unbiased manner and identified based on their spectral features. As collagen is the main organic constituent of bone [81], the increase in a collagen-rich tissue type derived from the spectral data strongly suggested the development of ectopic bone in scaffolds initially seeded with hMSCs. This tendency became apparent 4 weeks after implantation which may be related to differentiation of hMSCs into mature osteoblasts [82]. However, we did not observe the typical 960 cm^{-1} phosphate Raman band related to hydroxyapatite (HAp) [24], the main inorganic component of bone [81]. This is likely due to the overlapping strong phosphate bands of βTCP completely masking the weaker signal from the relatively low concentrations of HAp. Nevertheless, the presence of stem cell mediated bone was confirmed by histological analysis and μCT scans. It is interesting to notice that the proteinaceous collagen-like content (component 3 of the spectral unmixing) showed a similar time dependency for all engineering strategies during the first two to three weeks after implantation (Fig. 3b). We speculate this is due to a foreign-body response [83,84] resulting in an initial increase of protein in the subcutaneous pockets.

It should be noted, that despite βTCP being a bioresorbable synthetic bone substitute [5] the spectral analysis suggests no time-dependant degradation (Component 1, Fig. 3b). This is attributed to a lack of cell mediated degradation from osteoclasts in the immunodeficient mice.

Raman spectroscopy has previously been utilized for quantitative monitoring of tissue components in TE constructs *in vitro* using biochemical assays and linear regression [33]. This work expands the concept to *in vivo* live animal research and demonstrates the technique's ability to bridge to well-known methods such as histology. While the spectroscopic method presented here has the advantage of being non-invasive and non-destructive, the associated spectral data analysis provides only the concentration of biochemical components in arbitrary units. Thus, a validation of the spectral models and quantification using reference methods is needed. It should be noted that once the model is developed and validated it can be readily applied in future experiments for time-dependant monitoring of tissue formation. A major advantage for Raman spectroscopy as shown here is the ability to perform repeated measurements on the same animal allowing for a reduction of the number of experimental units needed in longitudinal studies.

Conclusion

Here, we demonstrate the use of a simple Raman spectroscopy system based on fibre optics for *in vivo* label-free, non-invasive monitoring of tissue formation in tissue engineering scaffolds. Using multivariate analysis, we show that bone scaffolds seeded with and without hMSCs implanted for 16 weeks in subcutaneous pockets in mice produced different spectral signatures related to different types of developing tissue. Scaffolds seeded with hMSCs prior to implantation were associated with collagen-rich tissue whereas a lipid rich tissue type formed within scaffolds without stem cells. These observations were supported by *ex vivo* μCT scans and histology revealing stem cell mediated bone development in cell seeded scaffolds and adipocytes in scaffolds without. The multivariate spectral analysis produced relative quantifications of the tissue content revealing the time-dependency of each biochemical component and statistically significant differences between experimental groups mimicking different tissue engineering strategies. In addition, the Raman derived measures of collagen content correlated well with histological measures. Together this emphasizes Raman spectroscopy as a promising *in vivo* monitoring modality for assessing and comparing tissue engineering strategies at the biochemical level. We believe the methodology can be further developed and tailored for a number of small animal subcutaneous implant models to study for example ectopic bone formation, tissue regeneration, and scaffold resorption dynamics. Furthermore, the ability to perform repeated measurements on the same animal, helps reduce the number of experimental units needed for longitudinal studies.

Data availability

The datasets generated during the current study are available from the corresponding author on reasonable request.

Declaration of Competing Interest

M.Ø.A. owns shares in Particle3D but otherwise the authors declare no competing interests.

Anders Runge Walther reports financial support was provided by Independent Research Fund Denmark. Morten Ostergaard Andersen reports a relationship with Particle 3D that includes: equity or stocks.

CRediT authorship contribution statement

Anders Runge Walther: Conceptualization, Investigation, Software, Formal analysis, Visualization, Writing – original draft, Writing – review & editing. **Nicholas Ditzel:** Conceptualization, Investigation, Resources, Formal analysis. **Moustapha Kassem:** Conceptualization, Resources, Writing – review & editing. **Morten Østergaard Andersen:** Conceptualization, Resources, Writing – review & editing, Supervision. **Martin Aage Barsøe Hedegaard:** Conceptualization, Resources, Writing – review & editing, Funding acquisition, Project administration, Supervision.

Acknowledgments

Supplementary materials

Supplementary material associated with this article can be found, in the online version, at doi:10.1016/j.bbiosy.2022.100059.

References

[1] Jessop ZM, Al-Sabah A, Francis WR, Whitaker IS. Transforming healthcare through regenerative medicine. BMC Med 2016;14:1–6. doi:10.1186/s12916-016-0669-4.

[2] Williams D. Benefit and risk in tissue engineering. Mater Today 2004;7:24–9. doi:10.1016/S1369-7021(04)00232-9.

[3] Place ES, Evans ND, Stevens MM. Complexity in biomaterials for tissue engineering. Nat Mater 2009;8:457–70. doi:10.1038/nmat2441.

[4] Mather ML, Morgan SP, Crowe JA. Meeting the needs of monitoring in tissue engineering. Regen Med 2007;2:145–60. doi:10.2217/17460751.2.2.145.

[5] Wagoner Johnson AJ, Herschler BA. A review of the mechanical behavior of CaP and CaP/polymer composites for applications in bone replacement and repair. Acta Biomater 2011;7:16–30. doi:10.1016/j.actbio.2010.07.012.

[6] Hannink G. J.J.C. Arts, Bioresorbability, porosity and mechanical strength of bone substitutes: what is optimal for bone regeneration? Injury 2011;42:S22–5. doi:10.1016/j.injury.2011.06.008.

[7] Blaker JJ, Gough JE, Maquet V, Notingher I, Boccaccini AR. *In vitro* evaluation of novel bioactive composites based on Bioglass-filled polylactide foams for bone tissue engineering scaffolds. J Biomed Mater Res 2003;67:1401–11. doi:10.1002/jbm.a.20055.

[8] Gentleman E, Fredholm YC, Jell G, Lotfibakhshaiesh N, O'Donnell MD, Hill RG, Stevens MM. The effects of strontium-substituted bioactive glasses on osteoblasts and osteoclasts *in vitro*. Biomaterials 2010;31:3949–56. doi:10.1016/j.biomaterials.2010.01.121.

[9] Fernandes HR, Gaddam A, Rebelo A, Brazete D, Stan GE, Ferreira JMF. Bioactive Glasses and Glass-Ceramics for Healthcare Applications in Bone Regeneration and Tissue Engineering. Materials (Basel) 2018;11:2530. doi:10.3390/ma11122530.

[10] Burdick JA, Prestwich GD. Hyaluronic acid hydrogels for biomedical applications. Adv Mater 2011;23:41–56. doi:10.1002/adma.201003963.

[11] Kharkar PM, Kiick KL, Kloxin AM. Designing degradable hydrogels for orthogonal control of cell microenvironments. Chem Soc Rev 2013;42:7335–72. doi:10.1039/c3cs60040h.

[12] Sathy BN, Daly A, Gonzalez-Fernandez T, Olvera D, Cunniffe G, McCarthy HO, Dunne N, Jeon O, Alsberg E, Donahue TH, Kelly DJ. Hypoxia Mimicking Hydrogels to Regulate the Fate of Transplanted Stem Cells. Acta Biomater 2019. doi:10.1016/J.ACTBIO.2019.02.042.

[13] Salzlechner C, Haghighi T, Huebscher I, Walther AR, Schell S, Gardner A, Undt G, da Silva RMP, Dreiss CA, Fan K, Gentleman E. Adhesive Hydrogels for Maxillofacial Tissue Regeneration Using Minimally Invasive Procedures. Adv Healthc Mater 2020. doi:10.1002/adhm.201901134.

[14] Tamaddon M, Burrows M, Ferreira SA, Dazzi F, Apperley JF, Bradshaw A, Brand DD, Czernuszka J, Gentleman E. Monomeric, porous type II collagen scaffolds promote chondrogenic differentiation of human bone marrow mesenchymal stem cells *in vitro*. Sci Rep 2017;7. doi:10.1038/srep43519.

[15] Gu BK, Choi DJ, Park SJ, Kim MS, Kang CM, Kim C-H. 3-dimensional bioprinting for tissue engineering applications. Biomater Res 2016;20:12. doi:10.1186/s40824-016-0058-2.

[16] Ember KJI, Hoeve MA, McAughtrie SL, Bergholt MS, Dwyer BJ, Stevens MM, Faulds K, Forbes SJ, Campbell CJ. Raman spectroscopy and regenerative medicine: a review. Npj Regen Med 2017;12:1–10. doi:10.1038/s41536-017-0014-3.

[17] Movasaghi Z, Rehman S, Rehman IU. Raman spectroscopy of biological tissues. Appl Spectrosc Rev 2007;42:493–541. doi:10.1080/05704920701551530.

[18] Brauchle E, Schenke-Layland K. Raman spectroscopy in biomedicine - non-invasive *in vitro* analysis of cells and extracellular matrix components in tissues. Biotechnol J 2013;8:288–97. doi:10.1002/biot.201200163.

[19] Jermyn M, Desroches J, Aubertin K, St-Arnaud K, Madore WJ, De Montigny E, Guiot MC, Trudel D, Wilson BC, Petrecca K, Leblond F. A review of Raman spectroscopy advances with an emphasis on clinical translation challenges in oncology. Phys Med Biol 2016;61:R370–400. doi:10.1088/0031-9155/61/23/R370.

[20] Santos IP, Barroso EM, Bakker Schut TC, Caspers PJ, Van Lanschot CGF, Choi DH, Van Der Kamp MF, Smits RWH, Van Doorn R, Verdijk RM, Noordhoek Hegt V, Von Der Thüsen JH, Van Deurzen CHM, Koppert LB, Van Leenders GJLH, Ewing-Graham PC, Van Doorn HC, Dirven CMF, Busstra MB, Hardillo J, Sewnaik A, Ten Hove I, Mast H, Monserez DA, Meeuwis C, Nijsten T, Wolvius EB, Baatenburg De Jong RJ, Puppels GJ, Koljenović S. Raman spectroscopy for cancer detection and cancer surgery guidance: translation to the clinics. Analyst 2017;142:3025–47. doi:10.1039/c7an00957g.

[21] Cordero E, Latka I, Matthäus C, Schie I, Popp J. In-vivo Raman spectroscopy: from basics to applications. J Biomed Opt 2018;23:1. doi:10.1117/1.jbo.23.7.071210.

[22] Cui S, Zhang S, Yue S. Raman Spectroscopy and Imaging for Cancer Diagnosis. J Healthc Eng 2018;2018. doi:10.1155/2018/8619342.

[23] Krafft C, Dietzek B, Popp J. Raman and CARS microspectroscopy of cells and tissues. Analyst 2009;134:1046. doi:10.1039/b822354h.

[24] Mandair GS, Morris MD. Contributions of Raman spectroscopy to the understanding of bone strength. Bonekey Rep 2015;4:1–8. doi:10.1038/bonekey.2014.115.

[25] Esmonde-White K. Raman spectroscopy of soft musculoskeletal tissues. Appl Spectrosc 2014;68:1203–18. doi:10.1366/14-07592.

[26] McManus LL, Burke GA, McCafferty MM, O'Hare P, Modreanu M, Boyd AR, Meenan BJ. Raman spectroscopic monitoring of the osteogenic differentiation of human mesenchymal stem cells. Analyst 2011;136:2471. doi:10.1039/c1an15167c.

[27] Hashimoto A, Yamaguchi Y, Da Chiu L, Morimoto C, Fujita K, Takedachi M, Kawata S, Murakami S, Tamiya E. Time-lapse Raman imaging of osteoblast differentiation. Sci Rep 2015;5:1–8. doi:10.1038/srep12529.

[28] Pudlas M, Brauchle E, Klein TJ, Hutmacher DW, Schenke-Layland K. Non-invasive identification of proteoglycans and chondrocyte differentiation state by Raman microspectroscopy. J Biophotonics 2013;6:205–11. doi:10.1002/jbio.201200064.

[29] Liao Z, Sinjab F, Nommeots-Nomm A, Jones J, Ruiz-Cantu L, Yang J, Rose F, Notingher I. Feasibility of Spatially Offset Raman Spectroscopy for In Vitro and In Vivo Monitoring Mineralization of Bone Tissue Engineering Scaffolds. Anal Chem 2017;89:847–53. doi:10.1021/acs.analchem.6b03785.

[30] Dooley M, Prasopthum A, Liao Z, Sinjab F, McLaren J, Rose FRAJ, Yang J, Notingher I. Spatially-offset Raman spectroscopy for monitoring mineralization of bone tissue engineering scaffolds: feasibility study based on phantom samples. Biomed Opt Express 2019;10:1678. doi:10.1364/boe.10.001678.

[31] Dooley M, McLaren J, Rose FRAJ, Notingher I. Investigating the feasibility of spatially offset Raman spectroscopy for in-vivo monitoring of bone healing in rat calvarial defect models. J Biophotonics 2020:1–10. doi:10.1002/jbio.202000190.

[32] Kunstar A, Leferink AM, Okagbare PI, Morris MD, Roessler BJ, Otto C, Karperien M, Van Blitterswijk CA, Moroni L, Van Apeldoorn AA. Label-free Raman monitoring of extracellular matrix formation in three-dimensional polymeric scaffolds. J R Soc Interface 2013;10:1–12.

[33] Bergholt MS, Albro MB, Stevens MM. Online quantitative monitoring of live cell engineered cartilage growth using diffuse fiber-optic Raman spectroscopy. Biomaterials 2017;140:128–37. doi:10.1016/j.biomaterials.2017.06.015.

[34] Pudlas M, Koch S, Bolwien C, Walles H. Raman spectroscopy as a tool for quality and sterility analysis for tissue engineering applications like cartilage transplants. Int J Artif Organs 2010;33:228–37.

[35] Albro MB, Bergholt MS, St-Pierre JP, Vinals Guitart A, Zlotnick HM, Evita EG, Stevens MM. Raman spectroscopic imaging for quantification of depth-dependent and local heterogeneities in native and engineered cartilage. Npj Regen Med 2018;3:3. doi:10.1038/s41536-018-0042-7.

[36] Bergholt MS, St-Pierre JP, Offeddu GS, Parmar PA, Albro MB, Puetzer JL, Oyen ML, Stevens MM. Raman spectroscopy reveals new insights into the zonal organization of native and tissue-engineered articular cartilage. ACS Cent Sci 2016;2:885–95. doi:10.1021/acscentsci.6b00222.

[37] Gough JE, Notingher I, Hench LL. Osteoblast attachment and mineralized nodule formation on rough and smooth 45S5 bioactive glass monoliths. J Biomed Mater Res 2004;68A:640–50. doi:10.1002/jbm.a.20075.

[38] Jell G, Notingher I, Tsigkou O, Notingher P, Polak JM, Hench LL, Stevens MM. Bioactive glass-induced osteoblast differentiation: a noninvasive spectroscopic study. J Biomed Mater Res - Part A 2008;86:31–40. doi:10.1002/jbm.a.31542.

[39] Conovaloff A, Wang H-W, Cheng J-X, Panitch A. Imaging growth of neurites in conditioned hydrogel by coherent anti-Stokes Raman scattering microscopy. Organogenesis 2009;5:231–7. doi:10.4161/org.5.4.10404.

[40] Gentleman E, Swain RJ, Evans ND, Boonrungsiman S, Jell G, Ball MD, Shean TAV, Oyen ML, Porter A, Stevens MM. Comparative materials differences revealed in engineered bone as a function of cell-specific differentiation. Nat Mater 2009;8:763–70. doi:10.1038/nmat2505.

[41] Boyd AR, Burke GA, Meenan BJ. Monitoring cellular behaviour using Raman spectroscopy for tissue engineering and regenerative medicine applications. J Mater Sci - Mater Med 2010;21:2317–24. doi:10.1007/s10856-009-3965-0.

[42] Borkowski L, Sroka-Bartnicka A, Polkowska I, Pawlowska M, Palka K, Zieba E, Slosarczyk A, Jozwiak K, Ginalska G. New approach in evaluation of ceramic-polymer composite bioactivity and biocompatibility. Anal Bioanal Chem 2017;409:5747–55. doi:10.1007/s00216-017-0518-0.

[43] Khmaladze A, Kuo S, Kim RY, Matthews RV, Marcelo CL, Feinberg SE, Morris MD. Human oral mucosa tissue-engineered constructs monitored by raman fiber-optic probe. Tissue Eng - Part C Methods 2015;21:46–51. doi:10.1089/ten.tec.2013.0622.

[44] Reddi AH. Role of morphogenetic proteins in skeletal tissue engineering and regeneration. Nat Biotechnol 1998;16:247–52. doi:10.1038/nbt0398-247.

[45] Agarwal R, García AJ. Biomaterial strategies for engineering implants for enhanced osseointegration and bone repair. Adv Drug Deliv Rev 2015;94:53–62. doi:10.1016/j.addr.2015.03.013.

[46] Bin Bae E, Park KH, Shim JH, Chung HY, Choi JW, Lee JJ, Kim CH, Jeon HJ, Kang SS, Huh JB. Efficacy of rhBMP-2 Loaded PCL/β -TCP/bdECM Scaffold Fabricated by 3D Printing Technology on Bone Regeneration. Biomed Res Int 2018;2018. doi:10.1155/2018/2876135.

[47] Scott MA, Levi B, Askarinam A, Nguyen A, Rackohn T, Kang T, Chia S, James AW. Brief review of models of ectopic bone formation. Stem Cells Dev 2012;21:655–67. doi:10.1089/scd.2011.0517.

[48] Trachtenberg JE, Vo TN, Mikos AG. Pre-clinical Characterization of Tissue Engineering Constructs for Bone and Cartilage Regeneration. Ann Biomed Eng 2015;43:681–96. doi:10.1007/s10439-014-1151-0.

[49] du Sert NP, Ahluwalia A, Alam S, Avey MT, Baker M, Browne WJ, Clark A, Cuthill IC, Dirnagl U, Emerson M, Garner P, Holgate ST, Howells DW, Hurst V, Karp NA, Lazic SE, Lidster K, MacCallum CJ, Macleod M, Pearl EJ, Petersen OH, Rawle F, Reynolds P, Rooney K, Sena ES, Silberberg SD, Steckler T, Würbel H. Reporting animal research: explanation and elaboration for the arrive guidelines 2.0, 2020. doi:10.1371/journal.pbio.3000411.

[50] Slots C, Jensen MB, Ditzel N, Hedegaard MAB, Borg SW, Albrektsen O, Thygesen T, Kassem M, Andersen MØ. Simple additive manufacturing of an osteoconductive ceramic using suspension melt extrusion. Dent Mater 2017;33:198–208. doi:10.1016/j.dental.2016.11.012.

[51] Jensen MB, Slots C, Ditzel N, Albrektsen O, Borg S, Thygesen T, Kassem M, Andersen MØ. Composites of fatty acids and ceramic powders are versatile biomaterials for personalized implants and controlled release of pharmaceuticals. Bioprinting 2018;10:1–10. doi:10.1016/j.bprint.2018.e00027.

[52] Simonsen JL, Rosada C, Serakinci N, Justesen J, Stenderup K, Rattan SI, Jensen TG, Kassem M. Telomerase expression extends the proliferative life-span and maintains the osteogenic potential of human bone marrow stromal cells. Nat Biotechnol 2002;20:592–6 [pii]. doi:10.1038/nbt0602-592.

[53] Abdallah BM, Haack-Sørensen M, Burns JS, Elsnab B, Jakob F, Hokland P, Kassem M. Maintenance of differentiation potential of human bone marrow mesenchymal stem cells immortalized by human telomerase reverse transcriptase gene despite of extensive proliferation. Biochem Biophys Res Commun 2005. doi:10.1016/j.bbrc.2004.11.059.

[54] Bentzon JF, Stenderup K, Hansen FD, Schroder HD, Abdallah BM, Jensen TG, Kassem M. Tissue distribution and engraftment of human mesenchymal stem cells immortalized by human telomerase reverse transcriptase gene. Biochem Biophys Res Commun 2005;330:633–40. doi:10.1016/j.bbrc.2005.03.072.

[55] Jafari A, Siersbaek MS, Chen L, Qanie D, Zaher W, Abdallah BM, Kassem M. Pharmacological Inhibition of Protein Kinase G1 Enhances Bone Formation by Human Skeletal Stem Cells Through Activation of RhoA-Akt Signaling. Stem Cells 2015;33:2219–31.

[56] Abdallah BM, Ditzel N, Kassem M. Assessment of Bone Formation Capacity Using In vivo Transplantation Assays: procedure and Tissue Analysis. in: J.J. Westendorf (Ed.). Osteoporosis Methods Mol Biol 2008:89–100 455th ed.. doi:10.1007/978-1-59745-104-8_6.

[57] Gao X, Cui Y, Levenson RM, Chung LWK, Nie S. In vivo cancer targeting and imaging with semiconductor quantum dots. Nat Biotechnol 2004;22:969–76. doi:10.1038/nbt994.

[58] Smith AM, Mancini MC, Nie S. Bioimaging: second window for in vivo imaging. Nat Nanotechnol 2009;4:710–11. doi:10.1038/nnano.2009.326.

[59] Matousek P, Stone N. Development of Deep Subsurface Raman Spectroscopy for Medical Diagnosis and Disease Monitoring. Chem Soc Rev 2016;45:1794–802. doi:10.1039/c5cs00466g.

[60] Stevens O, Iping Petterson IE, Day JCC, Stone N. Developing Fibre Optic Raman Probes for Applications in Clinical Spectroscopy. Chem Soc Rev 2016;45:1919–34. doi:10.1039/c5cs00850f.

[61] Directive 2006/25/EC. Off J Eur Union 2006;49:38–59.

[62] Walther AR, Andersen MØ, Dam CK, Karlsson F, Hedegaard MAB. Simple Defocused Fiber Optic Volume Probe for Subsurface Raman Spectroscopy in Turbid Media. Appl Spectrosc 2020;74:88–96. doi:10.1177/0003702819873933.

[63] Eilers PHC, Boelens HFM, Baseline Correction with Assymetric Least Squares Smoothing, 2005.

[64] Eilers PHC. A Perfect Smoother. Anal Chem 2003;75:3631–6. doi:10.1021/ac034173t.

[65] Felten J, Hall H, Jaumot J, Tauler R, De Juan A, Gorzsás A. Vibrational spectroscopic image analysis of biological material using multivariate curve resolution-alternating least squares (MCR-ALS). Nat Protoc 2015;10:217–40. doi:10.1038/nprot.2015.008.

[66] Barton SJ, Hennelly BM. An Algorithm for the Removal of Cosmic Ray Artifacts in Spectral Data Sets. Appl Spectrosc 2019;73:893–901. doi:10.1177/0003702819839098.

[67] Choquette SJ, Etz ES, Hurst WS, Blackburn DH, Leigh SD. Relative Intensity Correction of Raman Spectrometers: NIST SRMs 2241 through 2243 for 785nm, 532nm, and 488nm/514.5nm Excitation. Appl Spectrosc 2007;61:117–29. doi:10.1366/000370207779947585.

[68] Okagbare PI, Morris MD. Fluorocarbon fiber-optic raman probe for non-invasive raman spectroscopy. Appl Spectrosc 2012;66:728–30. doi:10.1366/12-06592.

[69] Bergholt MS, Duraipandian S, Zheng W, Huang Z. Multivariate reference technique for quantitative analysis of fiber-optic tissue raman spectroscopy. Anal Chem 2013;85:11297–303. doi:10.1021/ac402059v.

[70] Aminzadeh A. Fluorescence bands in the FT-Raman spectra of some calcium minerals. Spectrochim Acta - Part A Mol Biomol Spectrosc 1997;53:693–7. doi:10.1016/S1386-1425(96)01848-3.

[71] Berry MW, Browne M, Langville AN, Pauca VP, Plemmons RJ. Algorithms and applications for approximate nonnegative matrix factorization. Comput Stat Data Anal 2007;52:155–73. doi:10.1016/j.csda.2006.11.006.

[72] Rygula A, Majzner K, Marzec KM, Kaczor A, Pilarczyk M, Baranska M. Raman spectroscopy of proteins: a review. J Raman Spectrosc 2013;44:1061–76. doi:10.1002/jrs.4335.

[73] Czamara K, Majzner K, Pacia MZ, Kochan K, Kaczor A, Baranska M. Raman spectroscopy of lipids: a review. J Raman Spectrosc 2015;46:4–20. doi:10.1002/jrs.4607.

[74] De Aza PN, Santos C, Pazo A, De Aza S, Cuscó R, Artús L. Vibrational Properties of Calcium Phosphate Compounds. 1. Raman Spectrum of β-Tricalcium Phosphate. Chem Mater 1997;9:912–15. doi:10.1021/cm960425d.

[75] Zhu GY, Zhu X, Fan Q, Wan XL. Raman spectra of amino acids and their aqueous solutions. Spectrochim Acta Part a-Mol Biomol Spectrosc 2011;78:1187–95. doi:10.1016/j.saa.2010.12.079.

[76] Slots C, Jensen MB, Ditzel N, Hedegaard MAB, Borg SW, Albrektsen O, Thygesen T, Kassem M, Andersen MØ. Simple additive manufacturing of an osteoconductive ceramic using suspension melt extrusion. Dent Mater 2017;33:198–208. doi:10.1016/j.dental.2016.11.012.

[77] Dawson JI, Kanczler J, Tare R, Kassem M, Oreffo ROC. Concise review: bridging the gap: bone regeneration using skeletal stem cell-based strategies - where are we now? Stem Cells 2014;32:35–44. doi:10.1002/stem.1559.

[78] Wang EA, Rosen V, D'Alessandro JS, Bauduy M, Cordes P, Harada T, Israel DI, Hewick RM, Kerns KM, LaPan P. Recombinant human bone morphogenetic protein induces bone formation. Proc Natl Acad Sci 1990;87:2220–4. doi:10.1073/pnas.87.6.2220.

[79] Lysdahl H, Baatrup A, Foldager CB, Bünger C. Preconditioning Human Mesenchymal Stem Cells with a Low Concentration of BMP2 Stimulates Proliferation and Osteogenic Differentiation In Vitro. Biores Open Access 2014;3:278–85. doi:10.1089/biores.2014.0044.

[80] Marupanthorn A, Tantrawatpan C, Kheolamai P, Tantikanlayaporn D, Manochantr S. Bone morphogenetic protein-2 enhances the osteogenic differentiation capacity of mesenchymal stromal cells derived from human bone marrow and umbilical cord. Int J Mol Med 2017;39:654–62. doi:10.3892/ijmm.2017.2872.

[81] Weiner S, Wagner HD. THE MATERIAL BONE: structure-Mechanical Function Relations. Annu Rev Mater Sci 1998;28:271–98. doi:10.1146/annurev.matsci.28.1.271.

[82] Chen YQ, Liu YS, Liu YA, Wu YC, Del Álamo JC, Chiou A, Lee OK. Bio- chemical and physical characterizations of mesenchymal stromal cells along the time course of directed differentiation. Sci Rep 2016;6:1–12. doi:10.1038/srep31547.

[83] Onuki Y, Bhardwaj U, Papadimitrakopoulos F, Burgess DJ. A Review of the Biocompatibility of Implantable Devices: current Challenges to Overcome Foreign Body Response. J Diabetes Sci Technol 2008;2:1003–15. doi:10.1177/193229680800200610.

[84] Ward WK. A Review of the Foreign-body Response to Subcutaneously-implanted Devices: the Role of Macrophages and Cytokines in Biofouling and Fibrosis. J Diabetes Sci Technol 2008;2:768–77. doi:10.1177/193229680800200504.